Polar Oxides without Inversion Symmetry through Vacancy and Chemical Order

Joshua Young,[†,‡,¶,∥] Eun Ju Moon,[†,∥] Debangshu Mukherjee,[§] Greg Stone,[§] Venkatraman Gopalan,[§] Nasim Alem,[§] Steven J. May,[†] and James M. Rondinelli*,[‡,⊥]

[†]Department of Materials Science and Engineering, Drexel University, Philadelphia, Pennsylvania 19104, United States
[‡]Department of Materials Science and Engineering, Northwestern University, Evanston, Illinois 60208, United States
[§]Department of Materials Science and Engineering, Pennsylvania State University, University Park, Pennsylvania 16802, United States
[⊥]Materials Science Division, Argonne National Laboratory, Argonne, Illinois 60439, United States

S Supporting Information

ABSTRACT: One synthetic modality for materials discovery proceeds by forming mixtures of two or more compounds. In transition metal oxides (TMOs), chemical substitution often obeys Vegard's principle, and the resulting structure and properties of the derived phase follow from its components. A change in the assembly of the components into a digital nanostructure, however, can stabilize new polymorphs and properties not observed in the constituents. Here we formulate and demonstrate a crystal-chemistry design approach for realizing digital TMOs without inversion symmetry by combining two centrosymmetric compounds, utilizing periodic anion-vacancy order to generate multiple polyhedra that together with cation

order produce a polar structure. We next apply this strategy to two brownmillerite-structured TMOs known to display centrosymmetric crystal structures in their bulk, $Ca_2Fe_2O_5$ and $Sr_2Fe_2O_5$. We then realize epitaxial $(SrFeO_{2.5})_1/(CaFeO_{2.5})_1$ thin film superlattices possessing both anion-vacancy order and Sr and Ca chemical order at the subnanometer scale, confirmed through synchrotron-based diffraction and aberration corrected electron microscopy. Through a detailed symmetry analysis and density functional theory calculations, we show that A-site cation ordering lifts inversion symmetry in the superlattice and produces a polar compound. Our results demonstrate how control of anion and cation order at the nanoscale can be utilized to produce acentric structures markedly different than their constituents and open a path toward novel structure-based property design.
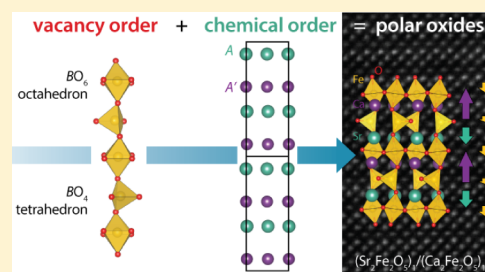
INTRODUCTION

Combining multiple compounds with desirable properties is a commonly pursued route to achieve functionality not found in either constituent material.[1,2] Although many systems follow a Vegard's law dependence in which the resultant mixture behaves as an approximate average of the two alloyed materials,[3,4] the deviation from such behavior can yield new insight into fundamental materials chemistry and new material platforms for applications. Marked examples include high-temperature superconductivity in $La_{2-x}Sr_xCuO_4$ oxides, where the parent La_2CuO_4 and $SrCuO_2$ compounds are insulators.[5] Hybrid perovskites are an illustrative second example, in which the combination of a salt and an organic molecule into the perovskite crystal structure leads to semiconducting compounds with photovoltaic responses markedly better than their parts.[6]

Toward realizing emergent properties from combinations of materials, the design of specific structural features can provide a direct means to target a desired functionality and reduce the need for serendipity.[7] This structure-driven approach to materials design is particularly useful in the discovery of new ferroelectrics and nonlinear optical materials with broken inversion symmetry, in which the functional property is directly coupled to structure and point symmetries.[8−11] In these compounds, the chemical mechanism responsible for polar displacements is usually due to the second-order Jahn−Teller effect;[12] however, the strict chemical criteria necessary for this mechanism to be operative (cations with either a d^0 or stereoactive ns^2 electron configuration)[13] severely restricts the material's chemistry and composition and often competes with other inversion-symmetry preserving distortions.[14] Moreover, combining multiple compounds in which inversion lifting arises from this mechanism typically results in polar behaviors that resemble an average of the constituents.[15,16]

An alternative, but still nascent, strategy for pursuing new acentric compounds focuses on layering *centrosymmetric* materials in a targeted manner that lifts inversion symmetry.[17] This approach has the added benefit of creating polar behavior while also retaining other electronic, magnetic or optical functionalities found in the constituent materials, thus enabling new multiferroics or narrow band gap polar semiconductors.
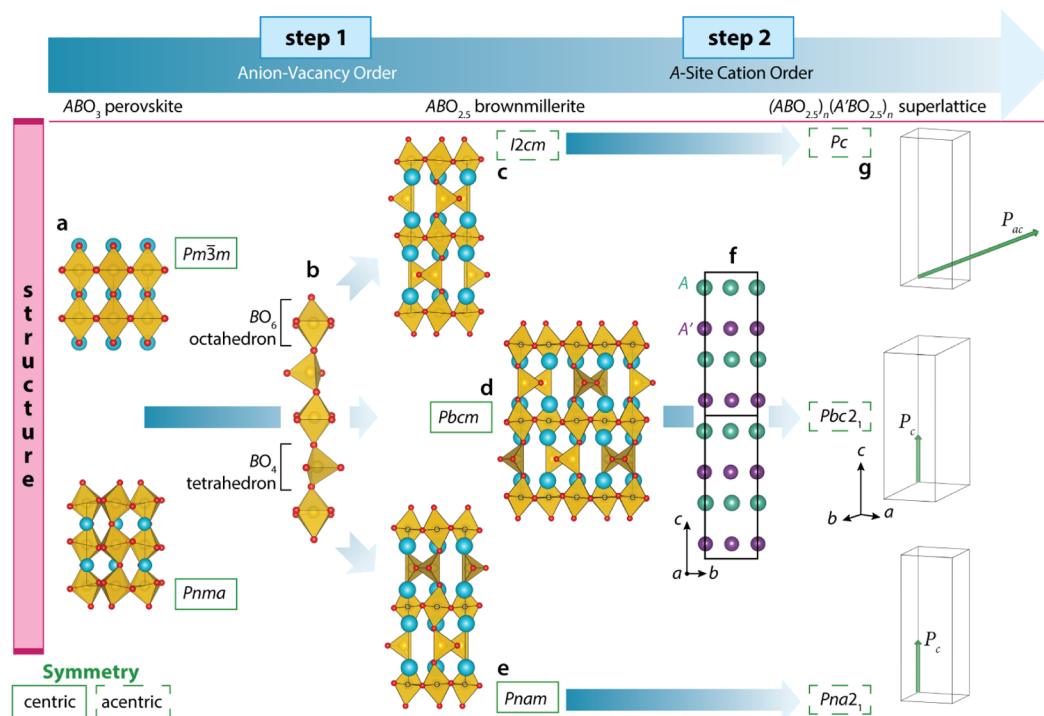
Figure 1. Design principles for realizing polar structures from nonpolar compounds through anion-vacancy and cation order. Starting from (a) fully oxidized perovskites are reduced in Step 1, resulting in (b) ordered rows of oxygen vacancies forming alternating layers of BO_6 octahedra and BO_4 tetrahedra. (c−e) Depict the resulting $ABO_{2.5}$ brownmillerites: the polar $I2cm$ and the nonpolar $Pbcm$ and $Pnam$ polymorphs that arise owing to the relative alignment of the BO_4 tetrahedra. Inversion centers are located at sites with octahedrally coordinated B cations, indicated by black open circles; not shown are the inversion centers located on the unoccupied sites in the $Pbcm$ and $Pnam$ polymorphs. (f) In Step 2, chemically distinct A and A' cations are ordered in layers along the $\cdots BO_6{-}BO_4{-}BO_6\cdots$ chain direction, which then removes all inversion centers and permits the net electric polarizations P indicated in (g).

Recent efforts in this vein have centered on geometric mechanisms in which cation ordering[18] combined with rotations of corner-connected octahedra result in noncentrosymmetric ABO_3 perovskite and $A_3B_2O_7$ Ruddlesden−Popper compounds.[19−26] Of particular relevance to this work, ordering of A-site cations in odd-period LaFeO₃/YFeO₃ superlattices was shown to lift inversion symmetry and produce a piezoelectric response,[25] while polar nanoregions were observed in oxygen deficient (LaFeO₃)₂/(SrFeO₃)₁ superlattices in sample areas that exhibited partial ordering of oxygen vacancies, with Fe displacements along the direction of the vacancy ordering.[27]

Here we present and employ a design strategy, which exploits both anion-vacancy order found in the $A_2B_2O_5$ brownmillerite structure and digital chemical ordering of A-site cations to form ultrashort-period superlattices through advanced layer-by-layer thin film deposition, for realizing polar materials. Using symmetry analyses, we first demonstrate that these site orders produce polar crystal structures. We then use density functional theory calculations to select optimal chemistries to fulfill these symmetry principles, identifying $(SrFeO_{2.5})_n/(CaFeO_{2.5})_n$ superlattices for experimentation. Although we focus on ferrite superlattices in this work, the broad chemistry-independent nature of this strategy means that it is applicable to numerous members of the brownmillerite family, such as manganites and cobaltites. Next, we realize the digitally ordered ferrite superlattices using molecular beam epitaxy (MBE) and confirm the materials exhibit both cation-chemical order and anion-vacancy order using synchrotron X-ray diffraction and scanning transmission electron microscopy (STEM). Through quantita-

tive analysis of the STEM images, we confirm the polar symmetry of the $n = 1$ superlattice, thereby verifying the approach. Last, we discuss the implications of anion-vacancy and cation order on the realization of new functional materials without inversion symmetry.

■ METHODS

Computational Methods. All investigations were performed using density functional theory as implemented in the Vienna Ab Initio Simulation Package (VASP).[28,29] We used projector augmented-wave (PAW) potentials[30] with the PBEsol functional,[31] a 550 eV plane wave cutoff, and a $7 \times 5 \times 7$ Monkhorst−Pack mesh.[32] We applied a Hubbard U correction of 5 eV using the Dudarev[33] formalism to treat the correlated Fe $3d$ states, and enforced a G-type antiferromagnetic collinear spin ordering on the Fe atoms. The electric polarization was calculated using the Berry phase method[34,35] as implemented in VASP, and the Born effective charge tensor was computed within density functional perturbation theory.

All $(SrFeO_{2.5})_1/(CaFeO_{2.5})_1$ structures were optimized under the following mechanical constraints to simulate thin film epitaxy on SrTiO₃. We fixed the in-plane lattice parameters of the three polymorphs to those of the SrTiO₃ substrate (3.905 Å), and relaxed the out-of-plane (c) lattice parameter and internal atomic positions until the forces on the atoms were less than 5×10^{-4} eV Å^{-1} and the stresses were less than 1×10^{-3} kB.

Material Synthesis. The brownmillerite $(SrFeO_{2.5})_n/(CaFeO_{2.5})_n$ superlattices and $(SrCa)_2Fe_2O_5$ random alloy films were grown with oxide MBE with Ca, Sr, and Fe sublimed from standard effusion cells. During deposition, the substrate temperature was held at ~ 500 °C, and O₂ was sourced to the substrate at a rate that yielded a chamber pressure of $\sim 2 \times 10^{-6}$ Torr. After deposition the samples were cooled in an O₂ pressure of $\sim 5 \times 10^{-7}$ Torr. The A-site and B-site cations were deposited simultaneously (codeposition) with each unit cell

followed by a 5 s pause, yielding a growth rate of ~25−35 s per unit cell. The atomic fluxes for the cation deposition were calibrated using Rutherford backscattering spectrometry.

Material Characterization. Synchrotron diffraction measurements were performed at the Advanced Photon Source at Sector 33-BM using a photon energy of 15 keV.

Electron transparent samples for electron microscopy were prepared using a FEI Helios NanoLab Dual-Beam Focused Ion Beam system, and were thinned down to 30 nm using a 30 kV Ga ion beam with final polishing being performed at 2 kV to remove the amorphous damage layer. The imaging was performed on a spherical aberration corrected FEI Titan[3] S/TEM at an operating voltage of 200 kV, with a probe convergence semiangle of 29 mrad, and the point resolution of 70 pm. ADF-STEM imaging was performed using Fischione detectors at a camera length of 115 mm, with an inner collection semiangle of 42 mrad, and an outer collection semiangle of 244 mrad. Images were collected with scanning directions parallel and perpendicular to the interface, and were subsequently corrected for scan drift.[36]

Convergent beam electron diffraction (CBED) experiments were performed using the FEI Titan[3], at an operating voltage of 80 kV, with a beam convergence angle of 3.2 mrad to separate the superlattice disks. Simulated CBED images for the [011] zone were calculated using the MacTempasX software up to a G_{max} of 1 Å^{-1}, with a 3 mrad convergence angle, a specimen thickness of 500 Å at an accelerating voltage of 80 kV.

■ RESULTS AND DISCUSSION

Design Principles. Lifting inversion symmetry requires that there is at least one unique anisotropic axis in the crystal along which the two ends are not related by any symmetry element, including an inversion center, a mirror plane, or a 2-fold rotation axis. We now formulate a design strategy to remove inversion centers by interleaving two centrosymmetric (CS) perovskites to generate derivative structures exhibiting site order on both the anion and cation lattices (Figure 1). We begin with a fully oxidized ABO_3 perovskite, which exhibits a three-dimensional corner connected BO_6 octahedral network. Figure 1a shows two of the most common perovskite polymorphs: the centric cubic $Pm\bar{3}m$ phase (with ideal octahedra) and the orthorhombic $Pnma$ phase (with rotated octahedra).

In Step (1), reduction of these compounds to $ABO_{2.5}$ (or equivalently, $A_2B_2O_5$) produces the derivative brownmillerite structure-type,[37] which possesses ordered chains of structural anion vacancies (Figure 1b). This oxygen vacancy order leads to a layered structure comprised of alternating corner-connected BO_4 tetrahedral chains and two-dimensional BO_6 layers along the c axis. Three polymorphs are possible owing to the fact that the tetrahedral chains can "rotate" with either a left- or right-handed sense. A polar $I2cm$ structure is possible if all of the chains are either left-handed or right-handed (Figure 1c). Two CS $Pbcm$ or $Pnam$ structures result if chains of different handedness are present, i.e., as a racemic mixture, and those chains alternate within each layer (Figure 1d) or alternate between each layer (Figure 1e), respectively. Both ordering of the anion-vacancies to form the BO_4 tetrahedra and the relative arrangements of the chain rotations stratifies the cation Wyckoff positions on the A and B sublattices of the brownmillerite structure (Supplementary Figure S1) such that only some of the B-cation positions retain a site symmetry with inversion as indicated by empty circles in Figure 1c,d. Finally, fully disordered tetrahedral chains, averaged over a macroscopic length scale, produce the centrosymmetric $Imma$ structure.

An examination of how different glide symmetry operations relate the tetrahedral chains both within each layer and along the c axis in each of the three distinct crystal structures reveals subtle but important differences. As indicated by the space group symmetry, the c-glide symmetry operation present in the $I2cm$ structure (i.e., reflection across a mirror plane perpendicular to the b axis, followed by a translation along c) maps the different tetrahedral layers, which all have the same handedness, onto each other. $Pbcm$, like $I2cm$, has a c-glide which relates the tetrahedral layers; however, it also displays a b-glide operation which changes the handedness of a tetrahedral chain across the reflection, and maps chains of different handedness within the same layer onto one another—note that this same type of handedness-changing operation is missing in the $I2cm$ space group. For the $Pnam$ polymorph, however, a single n-glide operation changes both the handedness of the tetrahedral chains and maps the different layers along the c axis onto one another, because each layer exhibits a tetrahedral-chain handedness that differs from those adjacent to it. Those within the same layer are then related by an a-glide. Finally, it is crucial to note that all three structures display a mirror plane perpendicular to the c axis which maps the different layers of A-site cations onto one another.

In Step (2), we use cation order to deterministically achieve a polar structure from these anion-vacancy ordered polymorphs by removing any remaining inversion-preserving operations. We order planes of A and A′ cations along the octahedral-tetrahedral direction alternating with a 1-to-1 periodicity (Figure 1f), giving a digital $(ABO_{2.5})_1/(A′BO_{2.5})_1$ superlattice. Although B-cation order is more frequently pursued in bulk brownmillerite compounds (see, e.g., refs 38 and 39), we find that A-site order is necessary to fully remove inversion. The oxygen vacancy order previously discussed shifts the inversion centers in these structures to positions that can only be broken with A-cation order (Supplementary Figure S1).

In all three brownmillerite crystal structures (Figure 1c, d, and e), 1-to-1 A-site cation order removes the mirror plane perpendicular to the tetrahedral-octahedral ordering axis (c). In $I2cm$, the mirror (and 2-fold rotation) symmetry is completely broken by cation ordering, resulting in a Pc space group; in $Pbcm$ and $Pnam$, the mirror plane is converted to a 2_1 screw axis, resulting in $Pbc2_1$ and $Pna2_1$, respectively. Consequently, net electric polarizations are permitted in all anion-vacancy and cation ordered superlattices (Figure 1g). Note that because the appearance of various glide planes originates from the tetrahedral chain handedness, they are not affected by the ordering and are preserved in the cation ordered superlattices. Similar symmetry reductions are possible with $n = 2$ superlattices (Supplementary Table S1). Because this design scheme relies solely on the static arrangement of the atoms in the crystal structure, regardless of their chemical makeup, it is applicable to any members of the brownmillerite family.

Application to Ferrites. We now apply these design principles to alkaline-earth ferrites, creating a digital $(SrFeO_{2.5})_1/(CaFeO_{2.5})_1$ heterostructure by interleaving the nonpolar bulk phases[40−43] of $Sr_2Fe_2O_5$ ($Pbcm$ symmetry) and $Ca_2Fe_2O_5$ ($Pnam$) along the c axis. Both bulk compounds are also established to be G-type antiferromagnets with Néel temperatures greater than 700 K owing to the d^5 electronic configuration of Fe^{3+}.[44−46] As described previously, the difference between these two crystal structures lies in the ordering of tetrahedral chains of different handedness. In $Pbcm$, the tetrahedral chains in different layers are related by a c-glide

symmetry operation, while those in the same layer are related by a *b*-glide; in *Pnam*, they are related by an *n*-glide and *a*-glide, respectively.

We first evaluate the energetic stability of the three possible polymorphs arising from the combination of the ordered oxygen vacancies (FeO_4 units) and the 1/1 superlattice periodicity using density functional theory (see Methods and Supplementary Table S2). Consistent with our schema, we find that the lowest energy structure is polar *Pbc2*$_1$, followed by *Pc* (2.6 meV/f.u. higher in energy) and *Pna2*$_1$ (6.3 meV/f.u. higher). The small energetic difference among polymorphs follows that reported for bulk $Ca_2Fe_2O_5$ and $Sr_2Fe_2O_5$[43] and suggests strong phase competition is possible.

All three structures exhibit small out-of-phase FeO_6 octahedral rotations that are present in $Ca_2Fe_2O_5$ and $Sr_2Fe_2O_5$. The FeO_4 tetrahedra between the three polymorphs are also very similar, with Fe−O bond lengths for the lowest energy *Pbc2*$_1$ structure (and the competing *Pc* structure) of 1.8340 (1.8325 Å), 1.8568 (1.8572 Å), 1.8987 (1.8998 Å), and 1.9017 (1.9038 Å), respectively. (Nearly identical bond lengths are found for the higher energy *Pna2*$_1$ structure as well.) Each digital $(SrFeO_{2.5})_1/(CaFeO_{2.5})_1$ superlattice also exhibits antipolar displacements of the Sr and Ca cations from their ideal positions along the ordering direction (*c* axis), resulting in a splitting of the interlayer Sr−Ca distances that are similar for all polar polymorphs (Figure 2). The separation between those *A*-site cations surrounding the octahedra is shorter (3.25 Å) than for those sur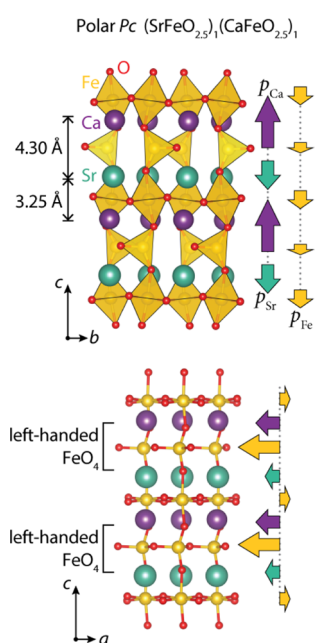rounding the tetrahedra (4.30 Å) but is comparable to the value obtained by taking an average of the same interlayer spacings in bulk $Sr_2Fe_2O_5$ and $Ca_2Fe_2O_5$.

Our calculations further predict the presence of a spontaneous electric polarization *P* arising from the asymmetric bond lengths induced by the *A*-site cation ordering and acentric FeO_4 tetrahedra. In the *Pbc2*$_1$, *Pc*, and *Pna2*$_1$ compounds, we find moderate polarizations along the out-of-plane *c* axis (P_c) of 4.93, 5.44, and 5.49 μC cm^{-2}, respectively. By comparing the relaxed structures to hypothetical undistorted reference phases with zero polarization, we can decompose the ionic contribution from each chemically distinct layer to the total polarization (Supplementary Table S3). In all three cases, we find that P_c originates from the aforementioned *A* cation displacements along the *c* direction of the alternating octahedral and tetrahedral layers (Supplementary Figure S2a). Although such displacements are present in the bulk compounds, they exactly cancel owing to the chemical homogeneity of the *A*-site cations (Supplementary Figure S2b) and the imposed mirror plane perpendicular to the *c* axis; in the digital heterostructure, however, the smaller Ca atoms displace more than Sr, and this noncancellation produces the observed out-of-plane polarization. Because the displacements of the *A* cations are similar in all polar polymorphs, the slight differences in net polarizations along P_c are a consequence of small distortions of the [4]- and [6]-coordinate Fe along the same axis, as indicated schematically for the *Pc* structure in Figure 2. Thus, identifying and quantifying the pattern and magnitude of the Fe displacements is essential to differentiating among the various polymorphs experimentally.

Furthermore, each of the three phases exhibits large displacements of tetrahedrally coordinated Fe atoms along the in-plane *a* direction. The presence of an equal amount of both left- and right-handed tetrahedral chains (which display exactly opposite Fe displacements) in the *Pbc2*$_1$ and *Pna2*$_1$ structures, however, results in a total cancellation of the polarization in this direction, i.e., $P_a = 0$ (Supplementary Figure S2c). In contrast, the chains are all of the same handedness in the monoclinic *Pc* phase; these cooperative displacements result in a large in-plane polarization of $P_a = 12.7$ μC cm^{-2} (Figure 1g and Figure 2).

Although the out-of-plane electric polarization originates from the uncompensated divalent *A* cation displacements, our electronic structure calculations reveal that the Born effective charges (BECs) for Sr and Ca are close to their nominal oxidation state (Supplementary Table S4). This behavior is a feature of geometric or hybrid improper ferroelectrics[47] and indicates that the combination of anion-vacancy order and cation order provide stability to the polar phase. Indeed, we show below that second-order Jahn−Teller activity is absent in the experimental superlattices. Finally, we computed the atom-resolved density of states (Supplementary Figure S3). We find that the electronic structure strongly resembles those of the constituent compounds,[43] with a band gap of 2.46 eV and a valence and conduction band made up primarily of O 2*p* and Fe 3*d* states, respectively.

Synthesis and X-ray Characterization. To verify the proposed design strategy, we grew the predicted brownmillerite $(SrFeO_{2.5})_n/(CaFeO_{2.5})_n$ superlattices with several periodicities (*n* = 1, 2, 4, 6, 10) and $(Ca,Sr)_2Fe_2O_5$ random alloy films on (001)-oriented $SrTiO_3$ substrates (STO, *a* = 3.905 Å) using oxide MBE. In monolithic films, STO would induce a 1.4% compressive strain in $Sr_2Fe_2O_5$ and a 0.2% tensile strain in $Ca_2Fe_2O_5$. In Figure 3a, we show synchrotron diffraction data

Figure 2. DFT optimized crystal structure for the *Pc* $(SrFeO_{2.5})_1/$ $(CaFeO_{2.5})_1$ superlattice depicting the layer polarizations, *p*, arising from Sr, Ca, and Fe displacements, designated, respectively as p_{Sr}, p_{Ca}, and p_{Fe}. The net polarization along the *c* axis (P_c component) originates mainly from the large p_{Ca} contribution, which is canceled by the oppositely aligned Sr layer polarization and the much smaller contributions from all Fe cations. The P_a component of the electric polarization is much larger; it is dominated by tetrahedral Fe displacements that are cooperative with both Ca and Sr. These layer polarizations are weakly compensated by the octahedral Fe contributions, which are antialigned to the other layer polarizations.

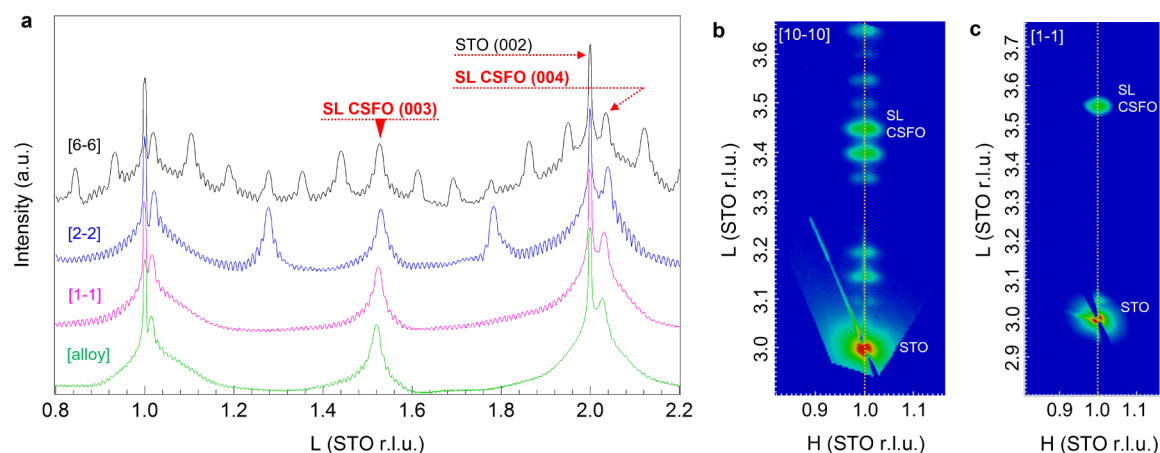**Figure 3.** Synchrotron diffraction measurement of $(SrFeO_{2.5})_n/(CaFeO_{2.5})_n$ superlattices. (a) Diffraction data along the (00L) rod in three superlattices, $n = 6, 2, 1$, and an alloy film grown on $SrTiO_3$ (STO) substrates; r.l.u. stands for reciprocal lattice units, which are given with respect to the STO substrate. Reciprocal space maps about the perovskite (113) Bragg reflection are shown for $n = 10$ and $n = 1$ superlattices in (b) and (c), respectively.
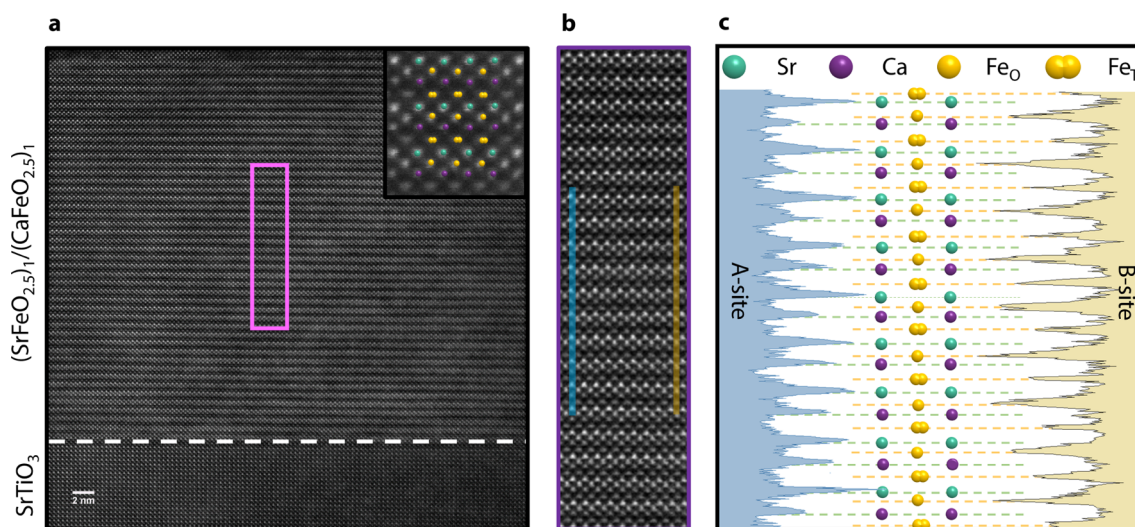

Figure 4. Confirmation of cation- and anion-vacancy orders with ADF-STEM measurements. (a) ADF-STEM image showing the $(SrFeO_{2.5})_1/(CaFeO_{2.5})_1$ superlattice on the $SrTiO_3$ substrate. Inset: Magnified image of a section of the film with atoms overlaid on top. The purple section in the film indicates the region used for the image intensity analysis. (b) Magnified section of the image denoted by the purple rectangle in (a) for image analysis, with the blue bar overlaid on top of A-site cations, and the yellow bar overlaid on top of B-site cations. (c) Intensity profiles along the A-sites and B-cation sites from regions shown in (b) corresponding to the atomic rows shown in the schematic.

collected along the (0 0 L) truncation rod of the alloy and the n = 1, 2, and 6 superlattices in reciprocal lattice units defined by the cubic STO lattice. A peak near (0 0 1.5) is observed for all samples, consistent with the (0 0 3) brownmillerite peak arising from the doubling of the unit cell along the c axis compared to the pseudocubic (pc) ABO_3 perovskite structure. Additional satellite peaks are observed for all superlattices with $n \geq 2$ as a consequence of the A-site cation ordering, which also contributes intensity to the (0 0 1.5) peak measured from the superlattices. In the $n = 1$ superlattice, the c-axis doubling induced by the Sr/Ca ordering also contributes to the (0 0 1.5) peak. However, due to the multiple structural features that double the c-axis within the $n = 1$ superlattice, we later provide STEM confirmation of the A-site ordering.

The vacancy ordering direction in epitaxial brownmillerite thin films is known to depend on the strain state,[48] with tensile and compressive strain favoring vacancy ordering along the [001] or [100] direction, respectively, in ferrite com-

pounds.[43,49−51] We confirmed the coherent strain state of the superlattices from reciprocal space maps around the (113) Bragg peak for the $n = 10$ and 1 superlattices, shown in Figure 3b and Figure 3c, respectively. The substrate and superlattice peaks occur at the same value of H indicating that the superlattices have the same in-plane lattice constant as STO, confirming an average tensile strain state within the super-lattices. Our observation of vacancy ordering along the [001] direction in the superlattices is therefore consistent with previous work on $Ca_2Fe_2O_5$ films under tensile strain,[50] a result that is somewhat surprising given that the magnitude of compressive strain within $Sr_2Fe_2O_5$ is larger than the tensile strain in $Ca_2Fe_2O_5$.

Polar Structure Determination. Annular dark field scanning transmission electron microscopy (ADF-STEM) was utilized to image the cation positions in the films and verify the polar crystal structure. First, we examined the presence of cation order throughout the superlattice. Figure 4a shows an
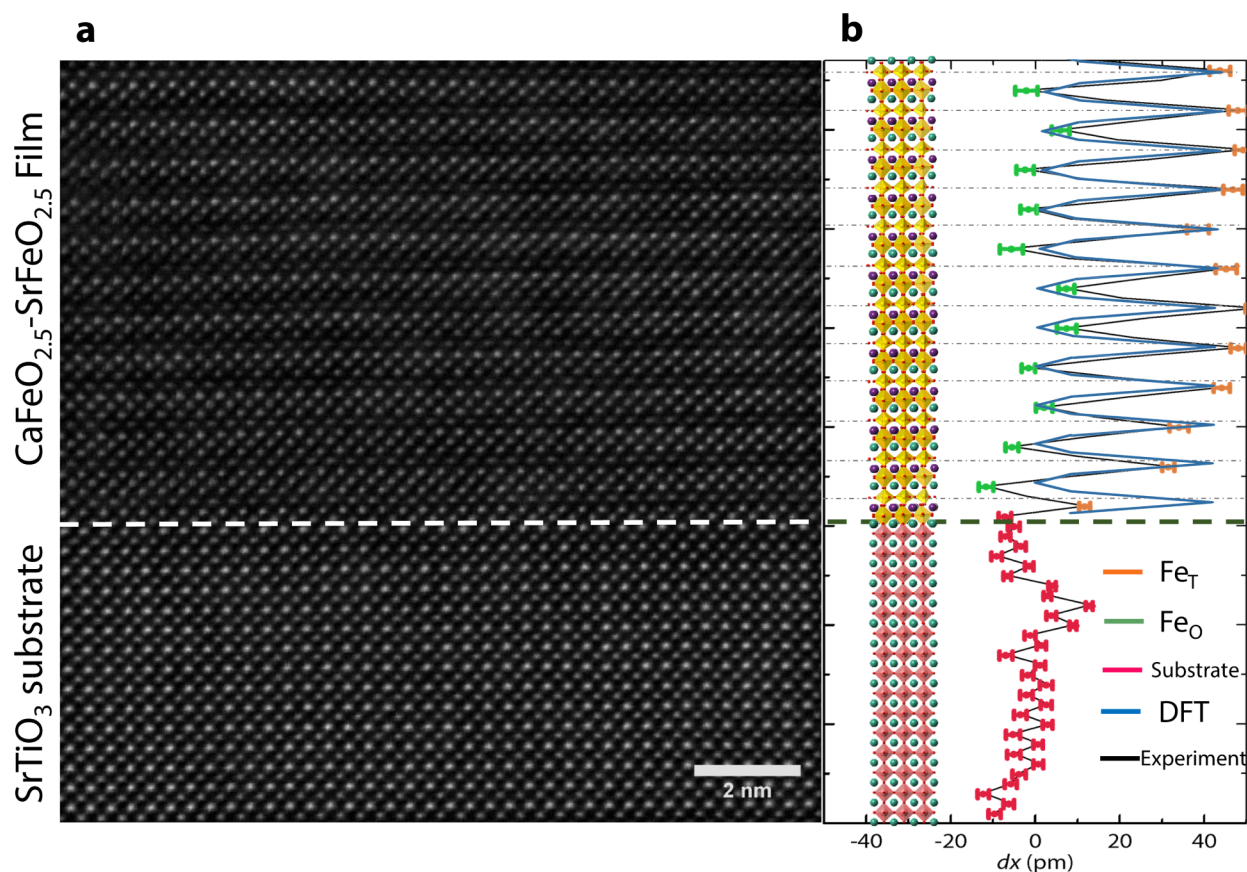
Figure 5. Cation displacements from high resolution STEM. Drift-corrected high resolution ADF-STEM image of a $(SrFeO_{2.5})_1/(CaFeO_{2.5})_1$ superlattice grown on $SrTiO_3$ and its measured B-site displacements in the horizontal direction. (a) High resolution ADF-STEM image of a $(SrFeO_{2.5})_1/(CaFeO_{2.5})_1$ superlattice, observed from the $(010)_{pc}$ zone, grown on a $SrTiO_3$ substrate along its (001) axis. (b) The corresponding schematic of the Pc crystal structure observed from the $(010)_{pc}$ zone grown on a (001) $SrTiO_3$ substrate is shown to the left. Measured layer-by-layer horizontal deviations from a cubic lattice are plotted to the right, with octahedrally (Fe_O) and tetrahedrally coordinated (Fe_T) iron layers in brown and blue, respectively, and the Ti displacements within the substrate marked in red. The DFT predicted horizontal displacements for the Pc structure, as calculated in Supplementary Figure S5, are overlaid as a solid blue line on top of the ADF-STEM experimentally measured displacements. Dashed-dotted gray lines connect the FeO tetrahedral layers in the STEM image to the aligned FeO layers in the crystal schematic and the corresponding measured horizontal displacements.

ADF-STEM image of the $n = 1$ brownmillerite superlattice on the $SrTiO_3$ substrate along the $(010)_{pc}$ zone axis, while Figure 4b shows a magnified portion of the structure. Intensity profiles were measured along the growth direction for both the A-site and B-site cations (Figure 4c); along the A-sites the higher (lower) intensity corresponds to the Sr (Ca) atomic columns. Superlattice ordering with a 1/1 periodicity is clearly observed in the A-site intensity profile, indicating that the cation order required for inversion symmetry breaking is achieved.

Unlike the perovskite structure, the A-site cations do not lie in the same plane as the apical oxygens in the brownmillerite structure. Instead, the A–A distances between layers is contracted across the BO_6 octahedra and expanded across the BO_4 tetrahedra as discussed previously. This difference in the A–A distances across the different polyhedra types is clearly discernible in the ADF-STEM images, Figure 4c. From the A-site intensity profile, the A–A interlayer distance across the BO_6 octahedra (d_O) and BO_4 tetrahedra (d_T) are determined to be 3.5 ± 0.1 Å and 4.3 ± 0.1 Å, respectively. These values of the A–A spacings are in good agreement with those obtained from simulations of the X-ray diffraction data ($d_O = 3.29$ Å and $d_T = 4.34$ Å), shown in Supplementary Figure S4 and the projected STEM spacings shown in Supplementary Figure S5. Both the

ADF-STEM and X-ray diffraction measured values closely match the DFT values of $d_O = 3.25$ Å and $d_T = 4.30$ Å, respectively. Unlike the octahedral layer, however, the Fe cations in the tetrahedral layer are not equidistant from the Sr and Ca planes; they are closer to the Sr layer by 0.1 Å. This noncancellation of Sr and Ca displacements arises as an effect of A-site cation ordering and substantiates the origin of the spontaneous out-of-plane polarization in these films.

The ordering of tetrahedral and octahedral Fe–O polyhedral units can be similarly distinguished. As predicted from density functional theory calculations, the Fe atoms of the tetrahedral layers undergo large alternating displacements. This gives rise to an in-plane separation of 0.54 Å of the tetrahedrally coordinated Fe atomic columns viewed along the $(010)_{pc}$, which is below the instrument resolution of the electron microscope. Hence the two neighboring Fe atomic columns are imaged as an elliptical intensity distribution in the ADF-STEM image (Figure 4c). In turn, the octahedrally coordinated Fe intensity distribution within the ADF-STEM image is circular, which has a side effect that the intensity of the octahedral Fe columns is higher than the tetrahedrally coordinated Fe atomic columns. This difference in displacement magnitude of the B-site cations manifesting in contrasting ADF-STEM intensity
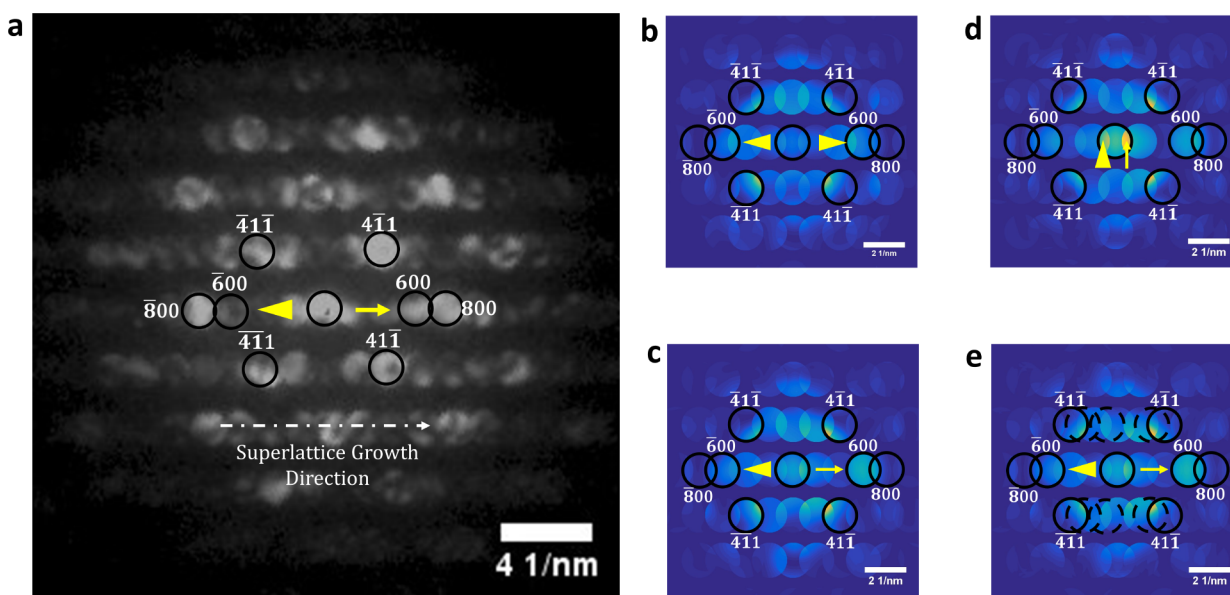
Figure 6. Confirmation of a polar structure with CBED. (a) Experimental CBED image obtained from the ⟨011⟩ Pc zone of the superlattice film with the diffraction disks labeled. The yellow arrow corresponds to the 600 zone with a higher observed intensity, as compared to the $\bar{6}00$ zone shown with the yellow triangle. (b) Simulated CBED pattern for the $Pnam$ $Ca_2Fe_2O_5$ structure showing the zones used for comparison with the superlattice. The 600 family of planes do not demonstrate intensity variation, and are thus both marked with yellow triangles. (c) Simulated CBED pattern for the Pc $(SrFeO_{2.5})_1/(CaFeO_{2.5})_1$ superlattice, showing higher intensity for the 600 disk as opposed to the $\bar{6}00$ disk. (d) Simulated CBED pattern for the $Pbc2_1$ $(SrFeO_{2.5})_1/(CaFeO_{2.5})_1$ superlattice, showing higher intensity for the 200 disk as opposed to the $\bar{2}00$ disk. (e) Simulated CBED pattern for the $Pna2_1$ $(SrFeO_{2.5})_1/(CaFeO_{2.5})_1$ superlattice, showing higher intensity for the 600 disk as opposed to the $\bar{6}00$ disk, with the extra diffraction disks appearing marked with dashed circles.

allows for clear discernment of the two distinct Fe chemical bonding environments present in the brownmillerite crystal structure.

We next used high resolution ADF-STEM imaging to verify the polar nature of the $n = 1$ superlattice through measurement of the cation displacements. Although our ab initio calculations predict three possible polar symmetries with distinct tetrahedral ordering schemes for the $n = 1$ superlattice—Pc, $Pbc2_1$ and $Pna2_1$—the three structures are distinguished by the displacement pattern of the tetrahedrally coordinated Fe atoms within the different layers. As discussed above, this relative displacement of the individual Fe atoms in-plane when viewed along $(010)_{pc}$ cannot be resolved. We therefore define dx as the average in-plane displacements of the cations with respect to the perovskite structure to make an assessment of the symmetry present. As shown in Supplementary Figure S5, the three structures can be distinguished based on the displacement patterns of the tetrahedrally coordinated Fe atoms. All dx values in the Pc crystal structure have the same sign (demonstrating that all of the tetrahedral chains exhibit the same handedness and the Fe atoms displace cooperatively), whereas in the $Pna2_1$ crystal structure the sign of dx reverses between neighboring layers (indicating antiparallel Fe displacements between tetrahedral layers). Finally, since each tetrahedral layer in the $Pbc2_1$ structure is a racemic mixture of left- and right-handed chains, the average dx values for each layer are zero.

Quantitative analysis of high-resolution ADF-STEM images, such as the one shown in Figure 5a, was then used to determine the crystal structure of the $(SrFeO_{2.5})_1/(CaFeO_{2.5})_1$ super-lattice. As shown in Figure 5b, the dx values in the substrate Ti layers are on the order of 0.05 Å, while the displacements of the tetrahedral Fe layers in the $(SrFeO_{2.5})_1/(CaFeO_{2.5})_1$ super-lattice are on the order of 0.40 Å, and are all aligned in the same direction. This cooperative displacement pattern thus indicates

that the films possess the Pc crystal structure, further confirming the polar nature of the superlattice.

The existence of polarity is present only in non-Laue point groups, where under dynamical diffraction conditions Friedel's rule is violated.[52,53] This was confirmed experimentally for the $(SrFeO_{2.5})_1/(CaFeO_{2.5})_1$ superlattice film with convergent beam electron diffraction (CBED) as shown in Figure 6a. The presence of features in the diffraction disks demonstrate dynamical diffraction, while the similar intensity profiles in the $[800]$ and $[\bar{8}00]$ disks show that tilt effects are minimal. However, the reversal of intensity across the $[\bar{6}00]$ and the $[600]$ disks demonstrate a violation of Friedel's rule, arising from the underlying absence of inversion symmetry in the film. Thus, a polar axis exists along the film growth direction, giving rise to an out of plane polar structure (Figure 2). CBED simulations confirm that the prototypical $Pnam$ brownmillerite $Ca_2Fe_2O_5$ structure does not demonstrate this asymmetry across the $[\bar{6}00]$ and the $[600]$ diffraction disks as shown in Figure 6b. Friedel's rule is however violated in the simulated CBED pattern for the Pc superlattice, as shown in Figure 6c where the $[600]$ disk exhibits a higher intensity when compared to the $[\bar{6}00]$ disk. This demonstrates that although the parent phase is centrosymmetric, cation ordering lifts the inversion symmetry as formulated by the design strategy.

Further Friedel asymmetries appear in both the $Pbc2_1$ and the $Pna2_1$ structures, as shown in Figure 6d and 6e, respectively, consistent with theory. Although the predicted polar axis remains the same in all three configurations, as shown in Figure 6d, for the $Pbc2_1$ structure, the asymmetry appears across the $[\bar{2}00]$ and the $[200]$ disks, corresponding to a higher polarization magnitude. Additionally, as Figure 6e demonstrates for the $Pna2_1$ structure, which is associated with antiparallel tetrahedral Fe displacements, extra reflections occur in the ⟨hkl⟩ planes when k is nonzero. The absence of higher order

peaks in the experimentally measured CBED pattern in Figure 6a, along with the asymmetry in the $\langle 600 \rangle$ disks, further supports the Pc structure assignment as measured by STEM (Figure 5).

CONCLUSION

Although the design and synthesis of ABO_3 perovskite superlattices with metastable cation layering has proven to be rich territory for engineering novel properties,[19,54−57] our results highlight the feasibility and promise of simultaneously *ordering both structural anion vacancies and cations* using advanced thin film deposition techniques as a new design strategy for realizing polar functional oxides. We note that the general behavior relies on the balance between site order and disorder, whereby configurational entropy will play a key role in this thermodynamic balance; however, a detailed formal treatment of these thermodynamics is beyond the scope of the present work. Furthermore, by successfully varying the ordering periodicity n, we have confirmed that the cation order can be precisely controlled in brownmillerite superlattices. The design strategy demonstrated here retains the functional properties of the $ABO_{2.5}$ constituent layers, thereby allowing for multifunctional combinations of polar behavior with physical properties found in the brownmillerite crystal class, such as robust magnetic ordering, semiconducting band gaps, and ionic conductivity.[41,46,58,59]

Finally, we note that the ability to deterministically realize polar structures in brownmillerite heterostructures may enable new functionalities not present in other improper ferroelectric systems. For example, previous work has demonstrated the ability to induce reversible topotactic transformations between ABO_3 and $ABO_{2.5}$ crystal structures in thin films at relatively low temperatures;[60,61] driving these oxidization and reduction reactions on $n = 1$ brownmillerite superlattices, such as with an electric field,[62,63] would enable new routes to manipulate polar phases with external stimuli. By building upon foundational advances in collective properties (e.g., superconducting cuprates[64]) with new theory-based design principles and state-of-the-art layer-by-layer growth techniques, novel compounds exhibiting technologically useful properties can be engineered from the atomic scale.

ASSOCIATED CONTENT

Ⓢ Supporting Information

The Supporting Information is available free of charge on the ACS Publications website at DOI: 10.1021/jacs.6b10697.

> Additional crystal structure details, dielectric properties, symmetry analyses, experimental characterization procedures, analyses, and larger field-of-view microscopy images (PDF)

AUTHOR INFORMATION

Corresponding Author

*jrondinelli@northwestern.edu

ORCID Ⓘ

James M. Rondinelli: 0000-0003-0508-2175

Present Address

¶J.Y.: Naval Research Laboratory, 4555 Overlook Avenue SW, Washington, D.C. 20375, United States.

Author Contributions

‖J.Y. and E.J.M. contributed equally to this work.

REFERENCES

(1) Chakhalian, J.; Freeland, J. W.; Millis, A. J.; Panagopoulos, C.; Rondinelli, J. M. *Rev. Mod. Phys.* **2014**, *86*, 1189−1202.

(2) O'Sullivan, M.; Hadermann, J.; Dyer, M. S.; Turner, S.; Alaria, J.; Manning, T. D.; Abakumov, A. M.; Claridge, J. B.; Rosseinsky, M. J. *Nat. Chem.* **2016**, *8*, 347−353.

(3) Vegard, L. *Eur. Phys. J. A* **1921**, *5*, 17−26.

(4) Denton, A. R.; Ashcroft, N. W. *Phys. Rev. A: At., Mol., Opt. Phys.* **1991**, *43*, 3161−3164.

(5) Lee, P. A.; Nagaosa, N.; Wen, X. G. *Rev. Mod. Phys.* **2006**, *78*, 17−85.

(6) Yang, W. S.; Noh, J. H.; Jeon, N. J.; Kim, Y. C.; Ryu, S.; Seo, J.; Seok, S. I. *Science* **2015**, *348*, 1234−1237.

(7) Rondinelli, J. M.; Poeppelmeier, K. R.; Zunger, A. *APL Mater.* **2015**, *3*, 080702.

(8) Bennett, J. W.; Rabe, K. M. *J. Solid State Chem.* **2012**, *195*, 21−31.

(9) Young, S. M.; Zheng, F.; Rappe, A. M. *Phys. Rev. Appl.* **2015**, *4*, 054004.

(10) Young, J.; Lalkiya, P.; Rondinelli, J. M. *J. Mater. Chem. C* **2016**, *4*, 4016−4027.

(11) Rondinelli, J. M.; Kioupakis, E. *Annu. Rev. Mater. Res.* **2015**, *45*, 491−518.

(12) Bersuker, I. B. *Chem. Rev.* **2013**, *113*, 1351−1390.

(13) Bersuker, I. B. *Phys. Rev. Lett.* **2012**, *108*, 137202.

(14) Benedek, N. A.; Fennie, C. J. *J. Phys. Chem. C* **2013**, *117*, 13339−133349.

(15) Vrejoiu, I.; Zhu, Y.; le Rhun, G.; Schubert, M. A.; Hesse, D.; Alexe, M. *Appl. Phys. Lett.* **2007**, *90*, 072909.

(16) Dawber, M.; Stucki, N.; Lichtensteiger, C.; Gariglio, S.; Ghosez, P.; Triscone, J.-M. *Adv. Mater.* **2007**, *19*, 4153−4159.

(17) Benedek, N. A.; Rondinelli, J. M.; Djani, H.; Ghosez, P.; Lightfoot, P. *Dalton Trans.* **2015**, *44*, 10543−10558.

(18) King, G.; Woodward, P. M. *J. Mater. Chem.* **2010**, *20*, 5785−5796.

(19) Bousquet, E.; Dawber, M.; Stucki, N.; Lichtensteiger, C.; Hermet, P.; Gariglio, S.; Triscone, J.-M.; Ghosez, P. *Nature* **2008**, *452*, 732−736.

(20) Benedek, N. A.; Fennie, C. J. *Phys. Rev. Lett.* **2011**, *106*, 107204.

(21) Rondinelli, J. M.; Fennie, C. J. *Adv. Mater.* **2012**, *24*, 1961−1968.

(22) Benedek, N. A.; Mulder, A. T.; Fennie, C. J. *J. Solid State Chem.* **2012**, *195*, 11−20.

(23) Young, J.; Rondinelli, J. M. *Chem. Mater.* **2013**, *25*, 4545−4550.

(24) Mulder, A. T.; Benedek, N. A.; Rondinelli, J. M.; Fennie, C. J. *Adv. Funct. Mater.* **2013**, *23*, 4810−4820.

(25) Alaria, J.; Borisov, P.; Dyer, M. S.; Manning, T. D.; Lepadatu, S.; Cain, M. G.; Mishina, E. D.; Sherstyuk, N. E.; Ilyin, N. A.; Hadermann, J.; Lederman, D.; Claridge, J. B.; Rosseinsky, M. J. *Chem. Sci.* **2014**, *5*, 1599−1610.

(26) Oh, Y. S.; Luo, X.; Huang, F.-T.; Wang, Y.; Cheong, S.-W. *Nat. Mater.* **2015**, *14*, 407−413.

(27) Mishra, R.; Kim, Y.-M.; Salafranca, J.; Kim, S. K.; Chang, S. H.; Bhattacharya, A.; Fong, D. D.; Pennycook, S. J.; Pantelides, S. T.; Borisevich, A. Y. *Nano Lett.* **2014**, *14*, 2694−2701.

(28) Hohenberg, P.; Kohn, W. *Phys. Rev.* **1964**, *136*, B864−B871.

(29) Kresse, G.; Furthmüller, J. *Comput. Mater. Sci.* **1996**, *6*, 15−50.

(30) Blöchl, P. E. *Phys. Rev. B: Condens. Matter Mater. Phys.* **1994**, *50*, 17953−17979.

(31) Perdew, J. P.; Ruzsinszky, A.; Csonka, G. I.; Vydrov, O. A.; Scuseria, G. E.; Constantin, L. A.; Zhou, X.; Burke, K. *Phys. Rev. Lett.* **2008**, *100*, 136406.

(32) Monkhorst, H. J.; Pack, J. D. *Phys. Rev. B* **1976**, *13*, 5188−5192.

(33) Dudarev, S. L.; Botton, G. A.; Savrasov, S. Y.; Humphreys, C. J.; Sutton, A. P. *Phys. Rev. B: Condens. Matter Mater. Phys.* **1998**, *57*, 1505.

(34) King-Smith, R. D.; Vanderbilt, D. *Phys. Rev. B: Condens. Matter Mater. Phys.* **1993**, *47*, R1651−R1654.

(35) Resta, R. *Rev. Mod. Phys.* **1994**, *66*, 899−915.

(36) Ophus, C.; Ciston, J.; Nelson, C. T. *Ultramicroscopy* **2016**, *162*, 1−9.

(37) Colville, A. A.; Geller, S. *Acta Crystallogr., Sect. B: Struct. Crystallogr. Cryst. Chem.* **1971**, *27*, 2311−2315.

(38) Ramezanipour, F.; Greedan, J. E.; Grosvenor, A. P.; Britten, J. F.; Cranswick, L. M. D.; Garlea, V. O. *Chem. Mater.* **2010**, *22*, 6008−6020.

(39) Didier, C.; Claridge, J.; Rosseinsky, M. *J. Solid State Chem.* **2014**, *218*, 38−43.

(40) Auckett, J. E.; Studer, A. J.; Sharma, N.; Ling, C. D. *Solid State Ionics* **2012**, *225*, 432−436.

(41) Auckett, J. E.; Studer, A. J.; Pellegrini, E.; Ollivier, J.; Johnson, M. R.; Schober, H.; Miiller, W.; Ling, C. D. *Chem. Mater.* **2013**, *25*, 3080−3087.

(42) Krüger, H.; Kahlenberg, V.; Petříček, V.; Phillipp, F.; Wertl, W. *J. Solid State Chem.* **2009**, *182*, 1515−1523.

(43) Young, J.; Rondinelli, J. M. *Phys. Rev. B: Condens. Matter Mater. Phys.* **2015**, *92*, 174111.

(44) Takeda, T.; Yamaguchi, Y.; Tomiyoshi, S.; Fukase, M.; Sugimoto, M.; Yamamoto, H. *J. Phys. Soc. Jpn.* **1968**, *24*, 446−452.

(45) Takeda, T.; Yamaguchi, Y.; Watanabe, J.; Tomiyoshi, S.; Yamamoto, H. *J. Phys. Soc. Jpn.* **1969**, *26*, 1320−1320.

(46) Schmidt, M.; Campbell, S. J. *J. Solid State Chem.* **2001**, *156*, 292−304.

(47) Young, J.; Stroppa, A.; Picozzi, S.; Rondinelli, J. M. *J. Phys.: Condens. Matter* **2015**, *27*, 283202.

(48) Klenov, D. O.; Donner, W.; Foran, B.; Stemmer, S. *Appl. Phys. Lett.* **2003**, *82*, 3427−3429.

(49) Rossell, M. D.; Lebedev, O. I.; van Tendeloo, G.; Hayashi, N.; Terashima, T.; Takano, M. *J. Appl. Phys.* **2004**, *95*, 5145−5152.

(50) Inoue, S.; Kawai, M.; Shimakawa, Y.; Mizumaki, M.; Kawamura, N.; Watanabe, T.; Tsujimoto, Y.; Kageyama, H.; Yoshimura, K. *Appl. Phys. Lett.* **2008**, *92*, 161911.

(51) Inoue, S.; Kawai, M.; Ichikawa, N.; Kageyama, H.; Paulus, W.; Shimakawa, Y. *Nat. Chem.* **2010**, *2*, 213−217.

(52) Nguyen, K. X.; Purohit, P.; Yadav, A.; Tate, M. W.; Chang, C. S.; Ramesh, R.; Gruner, S. M.; Muller, D. A. *Microsc. Microanal.* **2016**, *22*, 472−473.

(53) LeBeau, J. M.; D'Alfonso, A. J.; Wright, N. J.; Allen, L. J.; Stemmer, S. *Appl. Phys. Lett.* **2011**, *98*, 052904.

(54) Haeni, J. H.; Theis, C. D.; Schlom, D. G.; Tian, W.; Pan, X. Q.; Chang, H.; Takeuchi, I.; Xiang, X.-D. *Appl. Phys. Lett.* **2001**, *78*, 3292−3294.

(55) Sai, N.; Meyer, B.; Vanderbilt, D. *Phys. Rev. Lett.* **2000**, *84*, 5636−5639.

(56) Santos, T. S.; Kirby, B. J.; Kumar, S.; May, S. J.; Borchers, J. A.; Maranville, B. B.; Zarestky, J.; te Velthuis, S. G. E.; van den Brink, J.; Bhattacharya, A. *Phys. Rev. Lett.* **2011**, *107*, 167202.

(57) Yadav, A. K.; Nelson, C. T.; Hsu, S. L.; Hong, Z.; Clarkson, J. D.; Schlepütz, C. M.; Damodaran, A. R.; Shafer, P.; Arenholz, E.; Dedon, L. R.; Chen, D.; Vishwanath, A.; Minor, A. M.; Chen, L. Q.; Scott, J. F.; Martin, L. W.; Ramesh, R. *Nature* **2016**, *530*, 198−203.

(58) Zhang, G.; Smyth, D. *Solid State Ionics* **1995**, *82*, 161−172.

(59) Moon, E. J.; Choquette, A. K.; Huon, A.; Kulesa, S. Z.; Barbash, D.; May, S. J. *APL Mater.* **2015**, *3*, 062511.

(60) Poeppelmeier, K. R.; Leonowicz, M. E.; Longo, J. M. *J. Solid State Chem.* **1982**, *44*, 89−98.

(61) Jeen, H.; Choi, W. S.; Biegalski, M. D.; Folkman, C. M.; Tung, I.-C.; Fong, D. D.; Freeland, J. W.; Shin, D.; Ohta, H.; Chisholm, M. F.; Lee, H. N. *Nat. Mater.* **2013**, *12*, 1057.

(62) Tsuchiya, T.; Terabe, K.; Aono, M. *Appl. Phys. Lett.* **2013**, *103*, 073110.

(63) Lu, Q.; Yildiz, B. *Nano Lett.* **2016**, *16*, 1186−1193.

(64) Norton, D. P.; Chakoumakos, B. C.; Budai, J. D.; Lowndes, D. H.; Sales, B. C.; Thompson, J. R.; Christen, K. *Science* **1994**, *265*, 2074−2077.